

# Neutron Star Masses and Radii from Quiescent Low-Mass X-ray Binaries

James M. Lattimer

*Department of Physics and Astronomy, State University of New York at Stony Brook, Stony Brook, NY  
11794-3800, USA*

james.lattimer@stonybrook.edu

Andrew W. Steiner

*Institute for Nuclear Theory, University of Washington, Seattle, WA 98195, USA*

steiner3@uw.edu

## ABSTRACT

A recent analysis (Guillot et al. 2013) of the thermal spectra of 5 quiescent low-mass X-ray binaries in globular clusters, in which it was assumed that all neutron stars have the same radius, determined the radius to be  $R = 9.1_{-1.5}^{+1.3}$  km to 90% confidence. However, the masses of the sources were found to range from  $0.86 M_{\odot}$  to  $2.4 M_{\odot}$  and a significant amount of the predicted  $M - R$  region violates causality and the existence of a 2 solar mass neutron star. The study determined the amount of Galactic absorption along the lines-of-sight from fitting the X-ray spectra and assumed all sources possessed hydrogen atmospheres. We argue, from a Bayesian analysis, that different interpretations of the data are strongly favored. Our most-favored model assumes i) the equation of state of neutron star crusts is well-understood, ii) the high-density equation of state is consistent with causality and the existence of neutron stars at least as massive as  $2 M_{\odot}$ , iii) that the Galactic absorption is determined either from the fits in Guillot et al. (2013) or from independent HI surveys, and iv) that these objects are well-described by either hydrogen or helium atmospheres. With these assumptions, the 90% confidence radius range for  $1.4 M_{\odot}$  stars is 11.4 to 12.8 km, and the allowed range for radii of all neutron stars between  $1.2 M_{\odot}$  and  $2.0 M_{\odot}$  is 10.9 to 12.7 km. This result is in much greater agreement with predictions of the equation of state from both nuclear experiments and theoretical neutron matter studies than the smaller radii deduced by Guillot et al. (2013).

*Subject headings:* Dense matter — equation of state — stars: neutron, QLMXBs

## 1. INTRODUCTION

Although the masses of at least 3 dozen neutron stars have been relatively precisely measured (see Lattimer (2012) for a summary), estimates of individual neutron star radii are poorly known. Additionally, simultaneous mass and radius measurements for the same object are also relatively uncertain. The leading candidates for such measurements are bursting neutron stars that show photospheric radius expansion

(Van Paradijs 1979; Lewin, van Paradijs & Taam 1993) and transiently accreting neutron stars in quiescence (Rutledge et al. 1999), often referred to as quiescent low-mass X-ray binaries (QLMXBs). The former class of sources have the advantage that two relatively independent combinations of mass and radius are available, namely the Eddington luminosity associated with the maximum flux and the angular diameter ( $R_{\infty}/D$ ) inferred from the cooling tail of the burst, while latter class primarily measures the angular diameter and to

much lesser accuracy, their gravitational redshifts ( $z$ ). The source distance is  $D$ , and the radiation radius ( $R_\infty = R/\sqrt{1-2GM/Rc^2}$ ) and redshift ( $z = R/R_\infty - 1$ ) depend on the neutron star mass and radius,  $M$  and  $R$ , respectively. Unfortunately, photospheric radius expansion burst sources have large systematic errors including their distances, geometry of the bursting region, and compositions. In addition, they have been largely modeled (Özel, Güver & Psaltis 2009; Güver et al. 2010a,b; Özel, Baym & Güver 2010; Steiner, Lattimer & Brown 2010; Özel, Gould & Güver 2012; Suleimanov, Poutanen & Werner 2011; Steiner, Lattimer & Brown 2013) with static atmospheres but are certainly dynamical events. QLMXBs, on the other hand, have better-understood distances, but involve greater, and possibly more uncertain, amounts of interstellar absorption. And although they can be modeled as static atmospheres, the composition might be either hydrogen or helium (Rutledge et al. 1999).

The currently accepted theoretical explanation for the X-ray emission from QLMXBs is thermal energy deposited in the deep crust during outbursts Brown, Bildsten & Rutledge (1998). This energy further diffuses into and heats the core. Following outbursts, the energy is re-radiated on core-cooling timescales through the neutron star’s atmosphere. Accretion of heavier elements leads to their gravitational settling on timescales of seconds (Romani 1987; Bildsten, Salpeter & Wasserman 1992), thus the atmosphere is usually assumed to be pure hydrogen. Pure H atmosphere models (Rajagopal & Romani 2006; Zavlin, Pavlov & Shibano 1996; McClintock, Narayan & Rybicki 2004; Heinke et al. 2006; Haakonsen et al. 2012) applied to QLMXBs predict neutron star radii compatible with theoretical radius estimates, compared, for example, to blackbody models which would suggest  $R \lesssim 1$  km (Rutledge et al. 1999). Atmospheres dominated by heavier elements could occur when no hydrogen is accreted, such as is the case in some ultracompact X-ray binary systems like 4U 1820–30 where the donor is a helium white dwarf (Stella, Friedhorsky & White 1987; Rappaport, et al. 1987). Helium atmosphere models are generally less well understood, but recent works have begun to clarify how they impact radius constraints in QLMXBs (Servillat et al. 2012; Catuneanu et al. 2013). QLMXBs are ob-

served both in our Galaxy and in globular clusters, but distance uncertainties (or order 50%) associated with field sources precludes using them for accurate radius estimates. On the other hand, distance estimates to globular clusters can be  $\lesssim 10\%$ , making them ideal for radius and mass determinations.

A recent study of 5 QLMXBs by Guillot et al. (2013), hereafter G13, assuming that all the neutron stars have hydrogen atmospheres and the same radius, determined this radius to be  $R = 9.1_{-1.5}^{+1.3}$  km to 90% confidence. Given the importance of precisely measured neutron star radii for both astrophysics and nuclear physics (Lattimer & Prakash 2001; Steiner & Gandolfi 2012), we reconsider these 5 QLMXBs in the present study.

## 2. DATA AND FITS FOR QLMXBs

There have been multiple analyses of QLMXBs, but we will focus on 5 sources which were the subject of a recent analysis by G13. The observational data and results of spectral fitting of these sources with H atmospheres, both from G13 and previous studies, are summarized in Table 1. Utilizing the probability distributions from G13, kindly provided to us by S. Guillot, we modified the results for  $R_\infty$  attributed to G13 in this table to reflect distance uncertainties, which had not been done in the data provided (the values of  $z$  are not affected by distance uncertainties). In addition to the five sources studied by G13, we included, for comparison, previous analyses of the sources X7 in 47 Tuc and that in NGC 6553. G13, as well as previous studies, have made different assumptions about distances and hydrogen column densities (we denote the column density in units of  $10^{21}$  atoms  $\text{cm}^{-2}$  as  $N_{H21}$ ). One difference between G13 and many earlier studies is that G13 determine  $N_H$  together with the neutron star properties from spectral modeling while some of the other studies take its value from HI maps summarized by Dickey & Lockman (1990). For all sources, column 3 in Table 1 contains values of  $N_H$  according to the Chandra Proposal Planning Toolkit <http://cxc.harvard.edu/toolkit/colden.jsp>, hereafter referred to as CPPT, which lists Dickey & Lockman (1990) as its primary source. However, we note that the values for  $N_{H21}$  for M28, M13 and  $\omega$  Cen from the Chandra Toolkit and shown in col-

umn 3 slightly differ from those G13 attributed to Dickey & Lockman (1990) (G13 gives 2.4, 0.11 and 0.9, respectively, for these sources).

Three of the globular clusters, NGC 6397, M13 and  $\omega$  Cen, have dynamically-measured distances that are considered to be relatively reliable. M28 and NGC 6304 lack dynamical distance estimates. We use the distances and uncertainties given in G13, and also assume their errors can be modeled by a Gaussian probability distribution. Some previous works evaluated  $R_\infty$  based on different distance assumptions, and we have rescaled those values of  $R_\infty$  to reflect the G13 distances. In practice, the distance uncertainties are typically less than 10% and are not large enough to affect any of our conclusions.

G13 performed multiple sets of analyses, but we will discuss only three, of which just the second is displayed in Table 1. In G13’s first analysis, the most probable values for  $T_{\text{eff}}$ ,  $M$ ,  $R$  and  $N_H$  were evaluated for each source. Their second analysis fixed  $N_H$  to its most-probable value found in their first analysis, and redetermined the most-probable values for  $T_{\text{eff}}$ ,  $M$  and  $R$ . The values of  $T_{\text{eff}}$ ,  $M$  and  $R$  found in these two analyses are nearly indistinguishable except that the errors are typically less than half as much in the study in which  $N_H$  was fixed. The results from the fixed- $N_H$  study are displayed in Fig. 1 and summarized in Table 1, both now including distance uncertainties. Their third analysis was a joint analysis of all five sources under the assumption that  $R$  had the same value for each source. This analyses resulted in substantially different values of  $T_{\text{eff}}$  and  $M$ , and modestly different values of  $N_H$ , from the first analysis.

The probability distributions found by G13 tend to be banana-shaped, with the long axes approximately characterized by a fixed value of  $R_\infty$ . It is therefore useful to transform the  $M - R$  distributions into  $z - R_\infty$  distributions, again using the probability distributions from G13 provided to us by S. Guillot. The 90% confidence intervals for  $R$ ,  $M$ ,  $R_\infty$  and  $z$  are shown in Fig. 1 and summarized in the top row of column 8 of Table 1. An obvious feature of Fig. 1 is that the most-probable values of  $M$  and  $R$  for the 5 sources are roughly linearly related. This implies these sources have similar redshifts.

It should be noted that significant amounts of four of the five probability regions are for-

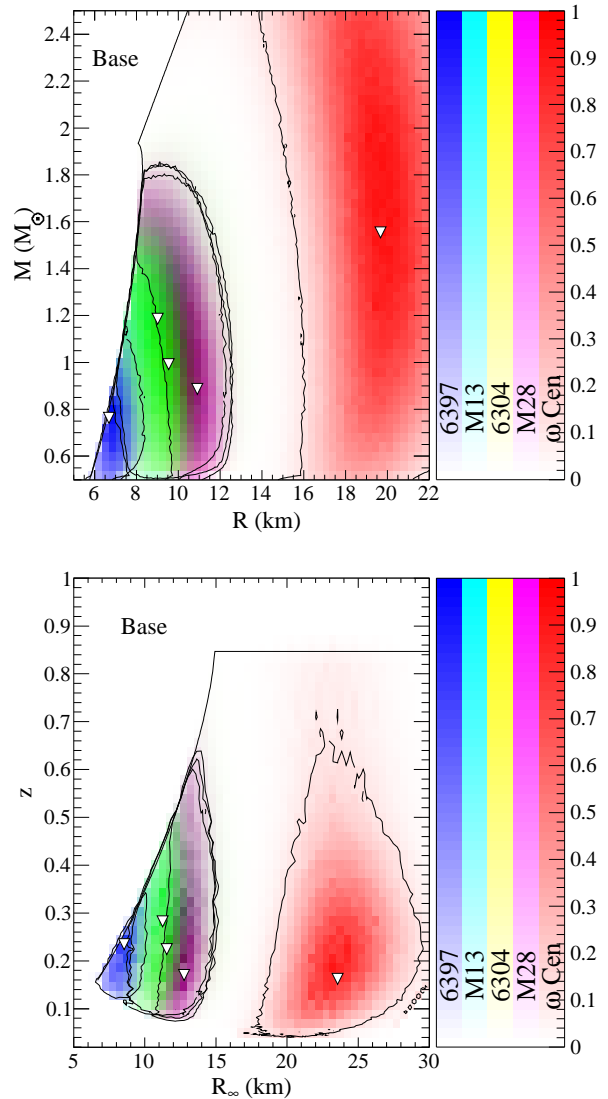


Fig. 1.— 90% error contours in  $R_\infty$  and  $z$  (top panel) and  $M$  and  $R$  (bottom panel) for QLMXRs studied by G13, including distance uncertainties. Triangles mark the most-favored values and contours bound 90% confidence regions. Triangle ordering in  $R_\infty$  or  $R$  is the same as the color bar ordering. Regions to the left of or above the solid lines are forbidden by the combination of causality and a  $1.93 M_\odot$  lower limit to the neutron star maximum mass. Shading densities are proportional to the probability density and colors from different sources are added together in RGB color space. Each color is renormalized to ensure that the red, green, and blue components attain their maximum value inside the plot. A black and white version is given in an Appendix.

TABLE 1  
PROPERTIES OF QLMXBs

Source	$D$ (kpc)	$N_{H21}$	$N_{H21}$	$R_\infty$ (km)	Ref.	$N_{H21}$	$R_\infty$ (km)	$z$
M28	$5.5 \pm 0.3$	1.89	$2.5 \pm 0.3$	$12.2 \pm 3.0$	(1)	2.52 (G)	$12.84^{+1.50}_{-1.48}$	$0.198^{+0.485}_{-0.120}$
			$2.6 \pm 0.4$	$14.5^{+6.9}_{-3.8}$	(2)	1.89	$10.65^{+1.27}_{-1.14}$	$0.212^{+0.456}_{-0.123}$
						1.89 (C)	$10.67^{+1.29}_{-1.16}$	$0.212^{+0.172}_{-0.116}$
NGC 6397	$2.02 \pm 0.18$	1.4	1.4	$9.6^{+0.8}_{-0.6}$	(3)	0.96 (G)	$8.42^{+1.32}_{-1.36}$	$0.242^{+0.278}_{-0.106}$
						1.4	$11.66^{+1.94}_{-1.72}$	$0.241^{+0.279}_{-0.102}$
						1.4 (C)	$11.68^{+2.00}_{-1.66}$	$0.241^{+0.213}_{-0.105}$
M13	$6.5 \pm 0.6$	0.145	0.11	$10.8 \pm 0.3$	(4)	0.08 (G)	$11.48^{+2.54}_{-2.29}$	$0.308^{+0.376}_{-0.212}$
			0.11	$12.3^{+1.4}_{-1.7}$	(5)	0.145	$12.93^{+2.91}_{-2.53}$	$0.286^{+0.392}_{-0.190}$
			0.12	$10.6^{+0.3}_{-0.4}$	(6)	0.145 (C)	$13.07^{+2.84}_{-2.51}$	$0.285^{+0.235}_{-0.184}$
$\omega$ Cen	$4.8 \pm 0.3$	1.04	0.9	$13.7 \pm 2.0$	(7)	1.82 (G)	$23.03^{+4.48}_{-3.86}$	$0.187^{+0.492}_{-0.144}$
			NGC 5139	$0.9 \pm 0.25$	$12.3 \pm 0.3$	(8)	1.04	$13.25^{+2.57}_{-2.08}$
NGC 5139			1.2	$13.9^{+6.5}_{-4.5}$	(6)	1.04 (C)	$13.29^{+2.55}_{-2.08}$	$0.200^{+0.266}_{-0.127}$
			NGC 6304	$6.22 \pm 0.26$	2.66	2.66	$12.1^{+6.6}_{-4.8}$	(9)
						2.66	$9.39^{+2.09}_{-1.75}$	$0.212^{+0.407}_{-0.108}$
						2.66 (C)	$9.54^{+2.13}_{-1.66}$	$0.212^{+0.141}_{-0.104}$
47 Tuc X7	$4.85 \pm 0.29$	0.53	$0.42^{+0.18}_{-0.16}$	$17.1^{+1.8}_{-1.5}$	(10)			
NGC 6553	6.0	3.64	3.5	$10.7^{+2.0}_{-1.5}$	(11)			

The distance  $D$  is that adopted by G13 and used to scale all results for  $R_\infty$ .  $N_H$  values in column 3 are taken from the Chandra Toolkit <http://cxc.harvard.edu/toolkit/colden.jsp>.  $N_H$  and  $R_\infty$  values in columns 4 and 5 are those quoted by the references cited in column 6: (1) – Servillat et al. (2012); (2) – Becker et al. (2003); (3) – Guillot, Rutledge & Brown (2011a); (4) – Gendre, Barret & Webb (2003b); (5) – Catuneanu et al. (2013); (6) – Webb & Barret (2007); (7) – Rutledge et al. (2002); (8) – Gendre, Barret & Webb (2003a); (9) – Guillot et al. (2009); (10) – Heinke et al. (2006); (11) – Guillot et al. (2011b). The first row of columns 7, 8, and 9 for each source contains  $N_H$ ,  $R_\infty$ , and  $z$  values from G13 (marked G) recomputed to include distance uncertainties. In the second row,  $N_H$  is set to Chandra Toolkit values and  $R_\infty$  is scaled accordingly to Table 2 ( $z$  is nearly unchanged by this procedure). The third row has results for  $R_\infty$  and  $z$  further corrected (C) for causality (see text). Uncertainties reflect 90% confidence, except for distance, whose uncertainty is 68%.

bidden by the combination of causality (i.e., restricting the speed of sound to be less than the speed of light), general relativity and observations (i.e., restricting the minimum maximum neutron star mass ( $\hat{M}$ ) to be larger than  $\hat{M} = 1.93 M_\odot$ , the  $1\sigma$  lower limit to the mass of pulsar PSR J1614-2230 (Demorest et al. 2010), the most massive precision measurement. (We note that, recently, an even larger maximum,  $\hat{M} = 1.97 M_\odot$ , has been found (Antoniadis et al. 2013), but its error bounds overlap with those of PSR J1614-2230 and, in any case, the change would be too small to make a significant difference.) The combination of general relativity and causality alone imposes the restrictions  $R > 2.83 GM/c^2$  and  $z < 0.847$  (Lattimer & Prakash 2007), but the radius limit is increased for  $M < \hat{M}$  (Lattimer 2012). This reduction in allowable parameter space alters the averages and standard deviations we find:  $z = 0.23 \pm 0.11$ ,  $R_\infty = 13.7 \pm 5.3$  km, and  $R = 11.3 \pm 4.5$  km, as shown in Table 2.

Another item important to note is that the column densities G13 determined by X-ray fitting, for the two most extreme sources in terms of their estimated radii, are significantly different from those independently determined from HI surveys (Dickey & Lockman 1990). G13 point out that varying the column density of heavily absorbed sources leads to large changes in their estimated radii. As an exercise, G13 alternatively recomputed fits assuming  $N_H$  values from Dickey & Lockman (1990) for NGC 6397 and  $\omega$  Cen, with the corresponding results for  $R_\infty$  given in the second row of column 8 for those sources in Table 1. The values of  $R_\infty$  were found to approximately scale with the relative values of  $N_H$ . As a result, the alternative values of  $R_\infty$  for these sources tend to cluster nearer to the values found for the other three sources. This suggests that a more consistent picture might emerge if  $N_H$  is determined from independent HI surveys rather than from X-ray fitting.

Despite the fact that the most-favored radii of the five sources had a wide range of values, nearly 15 km, in G13's first and second analyses, they carried out a third analysis with an assumption that all sources should have the same radius. One motivation for this assumption was the Bayesian analysis of Steiner, Lattimer & Brown (2010) of data from 4 PRE burst sources and 4 QLMXBs.

Utilizing parameterized EOSs, they found that the most-favored EOSs produced  $M - R$  trajectories with nearly constant radii for stars with masses ranging from 1 to 2  $M_\odot$ . The study of Steiner, Lattimer & Brown (2010) assumed a fixed EOS in the neutron star crust, for densities below about  $n_s/2$  where  $n_s \simeq 0.16 \text{ fm}^{-3}$  is the nuclear saturation density, and also that all valid EOSs must be causal at all densities and also capable of producing the most massive, precisely-measured, neutron stars. This mass, which we denote  $\hat{M}$ , was taken to be  $1.67 M_\odot$  from observations of PSR J1903+0327 (Freire et al. 2011). A later study (Steiner, Lattimer & Brown 2013) employed  $\hat{M} = 1.93 M_\odot$  from observations of PSR J1614-2230 (Demorest et al. 2010) with largely unchanged results. The nearly radius-independent  $M - R$  trajectory results from the fact that some sources had estimated  $R_\infty$  values smaller than about 14 km coupled with the incorporation of a known neutron star crust EOS, causality and  $\hat{M} \gg 1.5M_\odot$ .

The main focus of this paper will be to explore alternative interpretations of observations of QLMXBs, in which the treatment of column densities, atmospheric compositions, and neutron star structure are different than in G13.

Before examining the impact of alternative assumptions, however, it is worthwhile to further investigate the origin and magnitude of the apparent correlations between  $N_H$ , atmosphere composition, and  $R_\infty$ . We will first explore the role of  $N_H$  in the estimate of radii from blackbody spectra and then consider spectra from H and He atmospheres.

### 3. DEPENDENCE ON $N_H$ AND COMPOSITION

As already noted by G13, the determinations of  $M$  and  $R$  are very sensitive to assumptions for  $D$  and  $N_H$ . The direction of the change in inferred values of  $R_\infty$  is as expected: increasing  $N_H$  has the same qualitative effect as increasing  $D$ , and inferred values of  $M$  and  $R$ , as well as  $R_\infty$ , scale with the assumed distance. What is surprising is that the effect is quite large and that  $R_\infty$  increases nearly proportionally to the assumed value of  $N_H$ . In the case of NGC 6397, an increase in  $N_H$  by a factor of 1.55 produces an increase in  $R_\infty$  of a

TABLE 2  
AVERAGE VALUES FOR DIFFERENT ASSUMPTIONS

Assumptions	$M (M_{\odot})$	$R$ (km)	$R_{\infty}$ (km)	$z$
G13 $N_H$ , H	1.24±0.55	11.3±4.5	13.7±5.3	0.23±0.11
CPPT $N_H$ , H	1.07±0.33	9.7±1.6	11.8±1.9	0.23±0.11
CPPT $N_H$ , H + He	1.24±0.42	10.9±2.1	13.4±2.6	0.25±0.12

NOTE.—The mean and standard deviation of some relevant quantities over all five QLMXBs in the data set. All values reflect probability regions allowed by causality and  $\dot{M} = 1.93M_{\odot}$ .

factor 1.42, while in the case of  $\omega$  Cen, a decrease in  $N_H$  by a factor of 0.49 produces a decrease in  $R_{\infty}$  by a factor 0.51 (G13).

### 3.1. Blackbody Atmosphere

Because X-ray absorption by interstellar H is frequency-dependent, the inferred effective temperatures depend on assumptions concerning  $N_H$ . It is straightforward to estimate the magnitudes of changes in the inferred  $T_{\text{eff}}$  and  $R_{\infty}$  values for different assumptions concerning  $N_H$ . As a first illustration, we employ a blackbody model. A simplification the blackbody model provides is that the emergent spectrum is independent of gravity or redshift for a given total flux and observed peak energy. We will subsequently explore the effects of gravity when considering hydrogen and helium atmospheres.

The observed energy dependence of the flux from an absorbed blackbody with an effective temperature  $T$  obeys

$$F(E, T, N_H) = \alpha E^3 \frac{e^{-bN_{H21}/E^{8/3}}}{e^{E/kT} - 1}, \quad (1)$$

where  $\alpha$  is a constant and  $b \simeq 0.16 \text{ keV}^{8/3}$ . The term involving  $N_H$  represents the approximate effects of absorption (Wilms, Allen & McCray 2000). For a given effective temperature  $T$ , the maximum flux occurs at  $E_0$  where  $dF/dE = 0$ , or

$$3 - (E_0/kT)(1 - e^{-E_0/kT})^{-1} + (8/3)bN_{H21}E_0^{-8/3} = 0. \quad (2)$$

The solution of this equation leads to  $E_0 \gtrsim 3kT$  in general, so that the small exponential term can

be neglected, leading to

$$E_0 \simeq kT \left( \frac{9 + 8bN_{H21}E_0^{-8/3}}{3} \right). \quad (3)$$

The total observed flux is  $(R/D)^2 \int_{E_L}^{E_U} F(E)dE$ , where  $E_L \sim 0.3 \text{ keV}$  and  $E_H \simeq 10 \text{ keV}$  represent the low- and high-energy cutoffs of the X-ray detector response function.

To compare the effect of changing the amount of absorption on the inferred radius, we assume the total observed flux and the peak energy  $E_0$  are held fixed as  $N_H$  is changed. With these assumptions, changing the hydrogen column density from  $N_1 \equiv N_{1,H21}$  to  $N_2 \equiv N_{2,H21}$  will alter the inferred effective temperature from  $T_1$  to  $T_2$ :

$$\frac{T_2}{T_1} \simeq \frac{9E_0^{8/3} + 8bN_1}{9E_0^{8/3} + 8bN_2}, \quad (4)$$

where we neglected the factor  $1 - e^{-E_0/kT}$  from Eq. (2). Therefore, the effective temperature will decrease with an increase in assumed column density. Conservation of the observed flux and peak energy leads to the following relation between the inferred neutron star radii in the two cases:

$$\left( \frac{R_2}{R_1} \right)^2 = \frac{\int_{E_L}^{E_U} F(E, T_1, N_1)dE}{\int_{E_L}^{E_U} F(E, T_2, N_2)dE}. \quad (5)$$

The integrals in Eq. (5) can be approximately evaluated by the method of steepest descent, in which the lower and upper integration limits are extended to  $-\infty$  and  $\infty$ , respectively, and the integrand is replaced by a Gaussian centered at  $E_0$ ,

which leads to

$$\left(\frac{R_2}{R_1}\right)^2 \simeq \frac{F_1}{F_2} \sqrt{\frac{F_2'' F_1}{F_2 F_1''}}, \quad (6)$$

where  $F_1 \equiv F(E_0, T_1, N_1)$  and  $''$  indicates a second derivative evaluated at the peak energy. Approximately, we have

$$\begin{aligned} \frac{F_1}{F_2} &\simeq \exp\left[\frac{11b(N_2 - N_1)}{3E_0^{8/3}}\right], \\ \frac{F_2'' F_1}{F_2 F_1''} &\simeq \frac{27E_0^{8/3} + 88bN_2}{27E_0^{8/3} + 88bN_1}. \end{aligned} \quad (7)$$

An increase in  $N_H$  necessarily leads to an increase in  $R$ , since both factors in Eq. (7) are greater than unity. As a numerical example, for  $T_1 = 0.1$  keV,  $N_1 = 0.9$  and  $N_2 = 1.8$ , one finds  $E_0 \simeq 0.52$  keV,  $T_2 \simeq 0.070$  keV, and  $R_2/R_1 \simeq 5.35$ . The analytic expressions Eqs. (6) and (7) are accurate, in this case, to better than 1%. The radius ratio is to be compared to  $R_{2\infty}/R_{1\infty} \simeq 2$  found by G13 for hydrogen atmosphere models in the case of  $\omega$  Cen (Table 1).

### 3.2. Hydrogen Atmosphere

We next consider the case of a hydrogen atmosphere. The observed spectrum can be approximated by

$$\begin{aligned} F(E, T, N_H) &= \alpha'(T) E^3 (e^{\beta(E/T)^p} - 1)^{-1} \times \\ &\times e^{-bN_H 21/E^{8/3}}, \end{aligned} \quad (8)$$

where  $\alpha'$  now depends on  $T$ ,  $\beta \simeq 1.35$ , and  $p \simeq 5/7$ . The value for  $p$  comes from considerations of the competition between electron scattering and free-free absorption in a gray atmosphere, and  $\beta$  is obtained by fitting realistic hydrogen atmosphere models (Romani 1987; Zavlin, Pavlov & Shibanov 1996) with temperatures near 0.1 keV. We are grateful to Ed Brown for bringing this approximation to our attention. The effect of  $p < 1$  is to broaden the energy distribution, so that there is a larger fraction of high-energy photons emitted compared to a blackbody.

Justification for the value of  $p$  can be found by considering the competition between scattering and absorption in a hydrogen atmosphere. The electron scattering cross section  $\sigma_s$  is constant and, for energies near the peak of the spectrum, is

much greater than the free-free cross section  $\sigma_f$ , which depends on energy, density and temperature as  $\sigma_f \propto \rho T^{-1/2} E^{-3}$ . The total distance a photon travels before being absorbed is approximately  $\lambda_f = N\lambda_s$  where  $\lambda_{s,f} = (n_e \sigma_{s,f})^{-1}$  is the respective mean free path and  $n_e$  is the number density of electrons. For a random walk, the physical depth a photon travels before being absorbed is  $z = \lambda_s \sqrt{N} = \sqrt{\lambda_f \lambda_s}$ .

To allow for changes in density and temperature in the atmosphere, emerging photons of energy  $E$  originate from an approximate depth determined by

$$\tau(E) = \frac{N_A}{\mu_e} \int \sqrt{\sigma_s \sigma_f} \rho dz \simeq 1, \quad (9)$$

where  $N_A$  is Avogadro's number and  $\mu_e$  is the mean molecular weight per electron. From hydrostatic equilibrium,  $\rho dz = dp/g$  where  $g$  is the constant surface gravity. For a gray atmosphere,  $p \propto T^4 \propto \rho T$ . Eq. (9) can thus be expressed as

$$\int E^{-3/2} T^{13/4} dT \propto 1. \quad (10)$$

Therefore, the temperature  $T_a$  at the depth where emergent photons of energy  $E$  originate scales with energy as  $T_a \sim E^{2/7}$ . For a Planckian spectrum at large optical depths, the specific flux therefore behaves like

$$F_E \propto E^3 [e^{E/kT_a} - 1]^{-1} \propto E^3 [e^{\beta(E/kT)^{5/7}} - 1]^{-1}. \quad (11)$$

Calibrating the peak flux to model hydrogen atmospheres (Romani 1987; Zavlin, Pavlov & Shibanov 1996) allows determination of the specific flux in this approximation,

$$\begin{aligned} F_E &= 8.73 \cdot 10^{22} T^{0.2} E^3 \left[ e^{\beta(E/T)^{5/7}} - 1 \right]^{-1} \\ &\text{erg cm}^{-3} \text{ s}^{-1} \text{ keV}^{-1}, \end{aligned} \quad (12)$$

where  $E$  and  $T$  are in keV. Another analytic approximation was determined by McClintock, Narayan & Rybicki (2004), which is

$$\begin{aligned} F_E &= 5.26 \cdot 10^{23} T^{0.5} E^{2.5} e^{-\beta'(E/T)^{0.55}} \\ &\text{erg cm}^{-3} \text{ s}^{-1} \text{ keV}^{-1}, \end{aligned} \quad (13)$$

where  $\beta' = 3.573$ . Our approximation represents a better fit for  $T > 10^6$  K, which suggests an improved approximation might be found if  $p$  was

a monotonically increasing function of temperature. However, most of the sources under study have  $T > 10^6$  K, so we forego a better approximation and simply utilize Eq. (12) in the subsequent discussion. A simplification afforded by either of Eqs. (12) or (13) is that effects of gravity will be straightforward to approximate, which ceases to be the case when  $p$  is a temperature-dependent parameter.

Including the effects of absorption, the peak in the observed spectrum occurs when

$$E_0 \simeq T \left( \frac{9 + 8bN_{H21}E_0^{-8/3}}{3\beta p} \right)^{1/p}, \quad (14)$$

ignoring small exponential factors. For unabsorbed spectra,  $E_0/T$  therefore has a constant value,  $(3/\beta p)^{1/p} \simeq 4.9$ . Assuming the observed peak energy is fixed, the effective temperatures for two different assumed column densities are now related by

$$\frac{T_2}{T_1} \simeq \left( \frac{9E_0^{8/3} + 8bN_1}{9E_0^{8/3} + 8bN_2} \right)^{1/p}, \quad (15)$$

again ignoring small exponential factors. One can find the ratio of inferred radii using Eq. (5), where the approximations Eq. (6) and

$$\begin{aligned} \frac{F_1}{F_2} &\simeq \left( \frac{T_1}{T_2} \right)^{0.2} \exp \left[ \left( \frac{8}{3p} + 1 \right) b \frac{N_2 - N_1}{E_0^{8/3}} \right], \\ \frac{F_2'' F_1}{F_2 F_1''} &\simeq \frac{27pE_0^{8/3} + 8bN_2(8 + 3p)}{27pE_0^{8/3} + 8bN_1(8 + 3p)}, \end{aligned} \quad (16)$$

are relatively accurate. For values of  $T_1 = 0.1$  keV,  $N_1 = 0.9$  and  $N_2 = 1.8$ , we now find that  $R_2/R_1 \simeq 2.24$ , considerably smaller than the blackbody result, and near the result reported by G13 for realistic atmosphere simulations. The primary reason for a smaller radius increase, relative to the blackbody case, is that  $p < 1$ . It is found in this case that  $E_0 = 0.78$  keV and  $T_2 = 0.078$  keV.

The increase of inferred  $R$  with increasing  $N_H$  is quite sensitive to the temperature. Fig. 2 shows these changes for different base effective temperatures. The dotted curves show the approximate analytic results using Eqs. (15), (6), and (16). It can be seen that, despite the nearly linear relation between  $N_H$  and  $R_\infty$  deduced by G13 for NGC

6397 and  $\omega$  Cen, the linearity is accidental. In summary, the effects of appreciably changing  $N_H$  are magnified by relatively low effective temperatures, and furthermore are large only for highly obscured sources (i.e., for  $N_{H21} \gtrsim 1$ ).

Further confirmation that our approximate study correctly predicts the effects of varying H column densities can be found in studies of quiescent X-ray binaries in the field. For example, Rutledge et al. (2000) reported  $R_{\infty 2}/R_{\infty 1} = 0.43_{-0.21}^{+0.36}$  and  $T_2 \simeq 0.80$  for the source 4U 2129+47 when  $T_1 = 0.06$ ,  $N_1 = 2.8$  and  $N_2 = 1.7$ ; our semi-analytic approach gives  $T_2 = 0.078$  and  $R_2/R_1 = 0.39$ . Also, Rutledge et al. (1999) reported  $R_{\infty 2}/R_{\infty 1} = 5.3_{-2.1}^{+3.8}$  and  $T_2 \simeq 0.80$  for the source 4U 1608-522 when  $T_1 = 0.13$ ,  $N_1 = 8$  and  $N_2 = 15$ ; our semi-analytic approach gives  $T_2 = 0.090$  and  $R_2/R_1 = 4.0$ . Given that the 90% confidence interval for the reported radius ratios are greater than  $\pm 50\%$ , the agreement is satisfactory.

### 3.3. Helium Atmosphere

The case of a helium atmosphere follows similarly to that of the hydrogen case. As in the case of hydrogen, we expect that electron scattering opacities dominates the mean free path so the effective exponent  $p = 5/7$  can be assumed for the spectral shape. Suleimanov, Poutanen & Werner (2011) computed an array of spectral energy distributions of hydrogen and helium atmospheres as functions of temperature and gravity. Although these tables do not extend to temperatures below about 0.3 keV, comparison shows, for a given gravity, that helium atmospheres with temperatures approximately 13% smaller than hydrogen atmospheres have nearly identical energy distributions and peak energies. Therefore, a simple approximation to a helium atmosphere would be that of Eq. (8) with  $\beta \simeq 1.24$  instead of 1.35. In this case, fitting an observed spectrum with a helium, rather than a hydrogen, atmosphere, and requiring that the peak in the energy distribution remain unaltered, would lead to an inferred temperature decrease by 13% and a corresponding inferred radius increase by about 28%.

For comparison, Catuneanu et al. (2013) analyzed data from Chandra, XMM and ROSAT for the M13 QLMXB using hydrogen and helium atmospheres. They determined that fits with helium

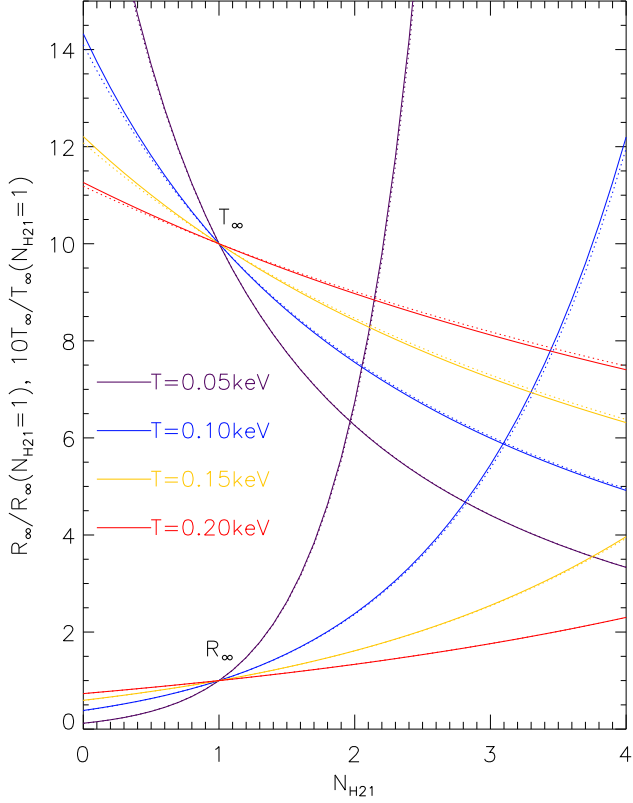


Fig. 2.— Radii (lower curves) and effective temperatures (upper curves) for hydrogen atmospheres as functions of column densities. Results are shown as ratios relative to the values obtained for the indicated base effective temperature and column density ( $N_{H21} = 1.0$ ). Solid lines show numerical results and dotted lines show the results of the analytical expressions discussed in the text.

atmospheres resulted in increases in radiation radii by a factor of approximately 1.25. However, because the helium fit involved a reduction in surface gravity, and as we show below, the effective value of  $\beta$  depends slightly on the assumed gravity, part of this radius change can be attributed to gravity effects. In contrast, Servillat et al. (2012) analyzed data for the M28 QLMXB and reported an increase in  $R_\infty$  of approximately 50% for a helium instead of hydrogen atmosphere. Their helium fit also resulted in a lower gravity than the hydrogen fit. We therefore estimate, for the calculations described below, that a change in atmospheric composition, at fixed gravity, from hydrogen to helium results in a radiation radius change of approximately 33%. At fixed redshift, these radius changes will necessarily result in gravity changes.

#### 4. DEPENDENCE ON GRAVITY AND REDSHIFT

To lowest order, hydrogen and helium atmospheres have a relatively weak dependence on gravity. The effects of gravity can be modeled as a small modification to the parameter  $\beta$  in Eq. (8). Without any temperature or gravity dependence in either  $\beta$  or  $\alpha'$ , the total integrated flux would be proportional to  $R^2 T^4$ , and after applying a source redshift, the observed flux becomes proportional to  $R_\infty^2 T_\infty^4$  which is the redshift-independent blackbody result. The net dependence on gravity stemming from gravity and temperature dependences in  $\alpha'$  and  $\beta$  allow, in principle, gravity or redshift information to be deduced from the spectrum.

The array of atmospheres computed by Suleimanov, Poutanen & Woźniak (2011) allows an estimate of the effect of gravity to be made. For the lowest temperatures they model, the effect of gravity on the spectral distributions for hydrogen atmospheres can be approximated with a gravity-dependent  $\beta$  parameter:

$$\beta \simeq 1.35 \left( \frac{g}{10^{14.3} \text{ cm}^2 \text{ s}^{-1}} \right)^{0.1}. \quad (17)$$

A similar change in the  $\beta$  factor for helium atmospheres is found. This gravity dependence is sufficiently weak that, to lowest order, it is safely ignored for the semi-analytic approximations discussed below. In support of this thesis, we note that in the comparison made by Servillat et al. (2012), replacing hydrogen by helium resulted in

an increase in  $R_\infty$  of about 50% but a reduction in  $1+z$  of only 4%.

In any case, other information in addition to the peak energy and total flux, such as higher moments, need to be considered in order to be able to obtain redshift constraints from spectral fitting. This accounts for the relatively large uncertainties in redshift estimated by G13 (Table 1). It also suggests that changes to assumed values of column density do not appreciably alter inferred redshifts of QLMXBs to leading order, so that we are somewhat justified in using the original values for  $z$  as computed by G13 when varying  $N_H$ . Nevertheless, these approximations make our analysis qualitative in nature, and moderate changes to neutron star properties can be expected from a more sophisticated analysis.

## 5. AN ALTERNATIVE INTERPRETATION OF QLMXBs

We now proceed by assuming that column densities are fixed by the independent observations of Dickey & Lockman (1990) when estimating neutron star properties from spectral fits. This necessitates rescaling the values of  $R_\infty$  from those determined by G13 and given in the first line for each source in Table 1. G13 have already performed this exercise for the neutron stars in NGC 6397 and  $\omega$  Cen, and their rescaled values for  $R_\infty$  are given in the second line for those sources in Table 1. In order to estimate analogous scaling corrections for the remaining three sources, we utilize the semi-analytic prescription discussed in §3.2. Table 3 shows the results of the above prescription applied to the sources in Table 1 for the two different assumed values of  $N_H$ . Our relatively simple representation of hydrogen atmospheres is seen to overpredict the changes in radii due to variations in column density when compared to the results of G13. It can be seen, however, that taking the  $2/3$  power of our predicted scaling factors for  $R_{\infty 2}/R_{\infty 1}$  in Table 3 rather closely represents the results of G13 for the sources NGC 6397 and  $\omega$  Cen. Therefore, this procedure has been used to modify the predicted radiation radii in the second row for the sources M28, M13 and NGC 6304 in Table 1. Only in the case of NGC 6304 is the correction appreciable. The third row for all five sources reflect the removal of probability

regions prohibited by general relativity, causality, and  $\hat{M} = 1.93M_\odot$ . (See the Appendix for some additional details on the how the correction is applied for  $\omega$  Cen.)

Using alternate values of  $N_H$ , we now find that the average radiation radius is  $R_\infty = 11.8 \pm 1.9$  km, yielding a mean radius  $R = 9.7 \pm 1.6$  km, after having removed those regions ruled out by causality (Table 2). The revised  $z - R_\infty$  and  $M - R$  90% confidence contours are displayed in Fig. 3. We note that the mean values of  $R$  and  $R_\infty$  have dropped by about 2 km, but their standard deviations have fallen by a factor of 2.8. On this basis, this procedure appears to be more plausible, and this will be tested using a Bayesian analysis in the next section.

The mean inferred radius in this analysis, which is below the expectations from nuclear experiments (although marginally overlapping the 90% confidence region reported by Lattimer & Lim (2013)), could be underestimated because it is possible that one or more of these QLMXB sources have helium, rather than hydrogen, atmospheres. Ultracompact binaries, which have neutron stars that have accreted helium or carbon atmospheres from white dwarf companions, are more likely to be found in globular clusters than in the field. Only in the cases of the neutron star in  $\omega$  Cen (Haggard et al. 2004), X5 in 47 Tuc (Heinke, Grindlay & Edmonds 2005) and several field sources has it been confirmed that the atmosphere is hydrogen. In particular, the abnormally small inferred value of  $R_\infty$  for the neutron star in NGC 6304, which challenges the causality plus maximum mass constraint, could be due to its having a helium, rather than a hydrogen, atmosphere.

As discussed in §3.3, we approximate the effect of helium by scaling the values of  $R_\infty$  shown in the third line of column 8 of Table 1 (i.e., the values found by G13 but corrected for causality and alternate values of  $N_H$ ) by 33% for all of the neutron stars except that in  $\omega$  Cen. We then add the resulting probability densities to those for the hydrogen atmosphere to get the full distribution which allows for either composition. In some cases,  $R_\infty$  is sufficiently well determined that this gives a clear bimodal form to the mass and radius. This is the case for the neutron star in M28 as shown in Fig. 4. Note that the peak hydrogen

TABLE 3  
EFFECTS OF VARYING  $N_H$

Source	$N_1$	$T_1$ (eV)	$R_{\infty 1}$ (km)	$N_2$	$T_2$ (eV)	$R_2/R_1$	$(R_2/R_1)^{2/3}$	$R_{\infty 2}/R_{\infty 1}^\ddagger$
	Guillot et al. (2013)			this work				
M28	2.52	119	$12.91^{+0.54}_{-0.61}$	$2.4^\ddagger$	121	0.949	0.965	
				$1.89^\dagger$	131	0.756	0.830	
NGC 6397	0.96	76	$8.40^{+0.32}_{-0.32}$	$1.4^\ddagger$	64	1.73	1.44	1.40
M13	0.08	86	$11.49^{+1.03}_{-0.97}$	$0.11^\ddagger$	83	1.09	1.06	
				$0.145^\dagger$	80	1.20	1.13	
$\omega$ Cen	1.82	64	$23.20^{+2.15}_{-2.08}$	$0.9^\ddagger$	87	0.371	0.516	0.511
				$1.04^\dagger$	82	0.433	0.572	
NGC 6304	3.46	106	$11.62^{+1.47}_{-1.26}$	$2.66^\ddagger$	118	0.713	0.800	

$^\dagger$ Dickey & Lockman (1990), <http://cxc.harvard.edu/toolkit/colden.jsp>;  $^\ddagger$ Guillot et al. (2013).

region of the probability distribution is noticeably higher than the peak of the helium region. We assume that hydrogen or helium are both equally probable and thus the integral of the probability density for each is equal. On the other hand, the helium region is broader because a larger value of  $R_\infty$  gives a larger mass range, thus the peak of the helium region must be lower.

The combined probability distributions for all five sources in this case are given in Fig. 5. We now find (Table 2) that the average radiation radius is  $R_\infty = 13.4 \pm 2.6$  km, yielding a mean radius  $R = 10.9 \pm 2.1$  km, after having removed those regions ruled out by causality.

## 6. EQUATION OF STATE AND $M - R$ CURVES FROM QLMXB DATA

We now proceed to perform the analysis of the QLMXB data using the Bayesian method described in Steiner, Lattimer & Brown (2010); Steiner, Lattimer & Brown (2013). In this analysis, the inferred observational data for these sources is confronted with additional constraints imposed by the assumption that the sources are neutron stars whose masses and radii are not free to vary independently but are related through the relativistic equations of stellar structure. An important aspect of this stems from

the assumption that the crustal EOS (i.e., that below about  $1.5 \cdot 10^{14}$  g cm $^{-3}$ ) is well understood. The EOS above that density is divided into three regions. The lowest of these density regions is described by an expansion of the nucleon energy per baryon in density and neutron excess around the nuclear saturation density ( $2.7 \cdot 10^{14}$  g cm $^{-3}$ ) and neutron-proton symmetry. The composition (i.e., the proton fraction) in this region is determined by beta equilibrium. In the baseline model, the upper two density regions are described with two polytropes (the model used in Steiner, Lattimer & Brown (2010) and also called model A in Steiner, Lattimer & Brown (2013)) that define the pressure as a function of energy density in beta equilibrium. This model is more appropriate for neutron stars without strong phase transitions and is labeled “Base” below. For neutron stars with strong phase transitions due to the appearance of exotic matter, such as from a quark-hadron phase transition, we instead employ discrete line segments in the pressure–energy density plane (model C in Steiner, Lattimer & Brown (2013) and labeled “Exo” below). The assumed division of the high-density EOS into three regimes is amply justified: Read et al. (2009) has demonstrated that the detailed EOS of a wide variety of strong interaction models is accurately predicted by three polytropic segments. In addition, we im-

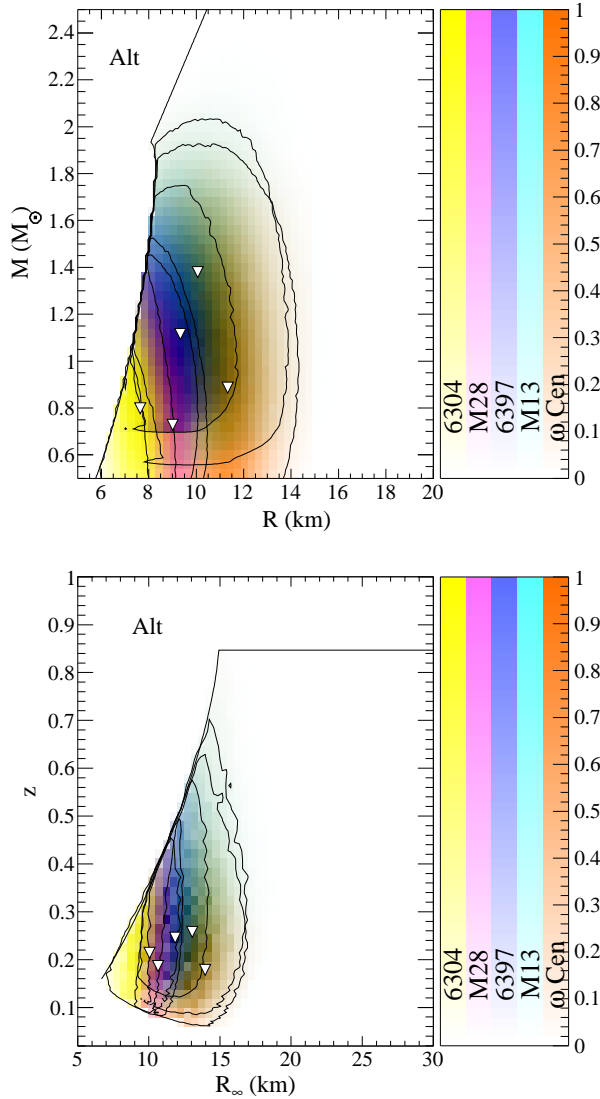


Fig. 3.— Similar to Fig. 1, but employing  $N_H$  values from Dickey & Lockman (1990) and the interpolation to scale  $R_{\infty}$  described in the text. A black and white version is given in an Appendix at the end.

pose constraints due to causality (i.e., that the speed of sound cannot exceed the speed of light) and the observational requirement that the neutron star maximum mass is greater than  $1.93 M_{\odot}$ . We also constrain neutron stars to be more massive than  $0.8 M_{\odot}$ , a conservative lower limit. In either case (Base or Exo), the allowable variations in the crustal EOS produce insignificant changes to our conclusions.

In contrast, G13 did not allow the radii of the five individual neutron stars to freely vary: they were assumed to have the same value which was determined by optimizing the fit to observational data. In this procedure, the correlations between masses and radii resulting from the stellar structure equations were largely ignored, and the strong constraints available from knowledge of the low-density EOS, causality, and the requirement  $\hat{M} \geq 1.93 M_{\odot}$ , were ignored. It was assumed that neutron stars are more massive than  $0.5 M_{\odot}$ . It is important to emphasize that G13 justifies their assumption that the radii of the five stars are equal on the basis that plausible EOSs predict that radii are insensitive to masses, for masses greater than  $0.5 M_{\odot}$ . In this sense, the approach we utilize is more rigorous because its implementation in Steiner, Lattimer & Brown (2010); Steiner, Lattimer & Brown (2013) led to the “constant radius” result that G13 assumes.

It should be emphasized, moreover, that the “constant radius” assumption is not necessarily valid, especially for EOSs that have strong phase transitions. Even EOSs without strong phase transitions, and with maximum masses satisfying observational values, predict radius variations  $\Delta R > 1 \text{ km}$  for  $0.5 M_{\odot} < M < 1.8 M_{\odot}$  and  $\Delta R > 2 - 3 \text{ km}$  for masses near the maximum mass, especially for EOSs with relatively large radii (see, e.g., Lattimer & Prakash (2001)). Note that these values of  $\Delta R$  are of the order of or greater than the predicted error in the radius deduced by G13.

A great advantage of our Bayesian analysis is that it allows one to compare in an unbiased way the quality of the models in terms of their fits to the observations. In the context of Bayesian statistics, a commonly accepted way of comparing two models is through the use of Bayes factors. Given a particular model,  $\mathcal{M}_{\alpha}$ , we can define the integral

$I_\alpha$  (sometimes called the evidence) as

$$I_\alpha \equiv \int P[\mathcal{D}|\mathcal{M}_\alpha] dp_1^{(\alpha)} dp_2^{(\alpha)} \dots dp_{N_p}^{(\alpha)} \times dM_1 dM_2 \dots dM_5 \quad (18)$$

where  $P[\mathcal{D}|\mathcal{M}_\alpha]$  is the conditional probability determined by the data and  $N_p$  is the number of parameters (denoted  $p^{(\alpha)}$ ) in the EOS parameterization. This notation is defined and further discussed in Steiner, Lattimer & Brown (2010). The outer integrations are over the neutron star masses (in this case, for five objects). (This integral is simplified because we assume uniform priors in both the EOS parameters and the neutron star masses.) The Bayes factor for comparing two possible models  $\alpha$  and  $\beta$  is then  $B_{\alpha,\beta} = I_\alpha/I_\beta$ . Typically, a Bayes factor of 10 would represent “strong” evidence that model  $\alpha$  is preferred to model  $\beta$  and 1/10 would be strong evidence of the opposite. A Bayes factor of 100 would be “decisive” for model  $\alpha$  over  $\beta$ . The integrals  $I$  for the models considered in this paper are given in Table 4, along with their uncertainties due to the interpolation used in the integration.

### 6.1. The Baseline Simulation

We use the original probability distributions for  $M$  and  $R$  given in G13 for fixed  $N_H$ , but include the distance uncertainty by folding in an additional uncertainty in  $R_\infty$  and also remove probability regions excluded by causality and  $\hat{M} \geq 1.93M_\odot$ . In this baseline simulation, which we label “Base”, we assume hydrogen atmospheres and consider the possibility of helium atmospheres below. The most probable radius as a function of mass is given in the upper panel of Fig. 6. The small mass and radius implied by the neutron star in NGC 6397 drive the simulation to small radii, but still larger (to 90% confidence, except for masses  $> 1.8M_\odot$ ) than the values  $7.6 \text{ km} < R < 10.4 \text{ km}$  determined by G13 under the assumption that the radii of all sources were equal. We attribute this to the implicit use of the stellar structure equations and knowledge of a crustal EOS in our simulation. In the baseline model, the radius of a  $1.4 M_\odot$  neutron star is near 11 km.

However, the Base model represents a very poor fit to the data. In particular, the predicted masses

and radii for the neutron stars in  $\omega$  Cen and NGC 6397 are far outside of their most probable regions when they are individually analyzed. For example, the most probable mass for the neutron star in  $\omega$  Cen is driven to  $2 M_\odot$  and the radius to 10 km, just at the edge of the region allowed by causality, compared to  $1.6 M_\odot$  and 20 km, respectively, in its individual analysis (Figure 1). In contrast, G13 obtains even more extreme parameters for this same object: the most probable mass is  $2.4 M_\odot$  (with all neutron star radii at 9.1 km), which lies outside the causally-allowed region.

Our results with exotic matter (lower panel of Fig. 6, model “Exo”) imply smaller radii, because of the presence of strong phase transitions (as observed in Steiner, Lattimer & Brown (2013)). Note also that this model has a bimodal distribution, predicting two different classes of radii for a fixed mass. This comes from the conflict between matching the neutron star in NGC 6397, which has a small value of  $R_\infty$ , with the neutron star in  $\omega$  Cen, which has a large value. The  $M - R$  curve be forced to fit both, so it fits one or the other.

The mean and standard deviation of the masses, radii, radiation radii, and redshifts for these two models are given in the first two rows of Table 4. Note that in either case, the standard deviations are substantially smaller than for the averages of the individual analyses as displayed in Table 2 for the G13  $N_H$ , H case. Note that the Bayes factor comparing these two models,  $B_{\text{Exo,Base}} = 1310 \pm 100$ , implies decisive evidence for a strong phase transition in neutron star matter. This result is clearly driven by the predicted small values of  $R_\infty$  for the neutron stars in NGC 6397, NGC 6304, and M13.

### 6.2. Alternate $N_H$ Simulations

We now consider models with the alternative assumptions about  $N_H$  (Alt). The corresponding  $M - R$  curves after having modified  $R_\infty$  according to the prescription described in §5 are given in Fig. 7. As is clear in the third and fourth rows of Table 4, the implied masses and radii are slightly smaller since most of the alternate  $N_H$  values imply a decrease in  $R_\infty$ . The Bayes factor comparing the normal and exotic EOS assumptions,  $B_{\text{Exo/Alt,Alt}} = 140 \pm 25$ , again implies that strong phase transitions are present. In order to compare these results to the models employing the G13 val-

TABLE 4  
PROPERTIES THE BAYESIAN MODELS

Model	$M (M_{\odot})$	$R$ (km)	$R_{\infty}$ (km)	$z$	$I$
Base	$1.31 \pm 0.40$	$11.09 \pm 0.39$	$13.8 \pm 1.1$	$0.25 \pm 0.12$	$(7.32 \pm 0.37) \times 10^{-9}$
Exo	$1.31 \pm 0.43$	$9.68 \pm 0.64$	$12.6 \pm 1.8$	$0.31 \pm 0.16$	$(9.60 \pm 0.57) \times 10^{-6}$
Alt	$1.17 \pm 0.26$	$11.02 \pm 0.33$	$13.2 \pm 0.7$	$0.21 \pm 0.07$	$(5.83 \pm 0.36) \times 10^{-3}$
Exo/Alt	$1.17 \pm 0.26$	$9.81 \pm 0.44$	$12.1 \pm 0.9$	$0.25 \pm 0.08$	$(8.19 \pm 1.35) \times 10^{-1}$
H+He	$1.42 \pm 0.41$	$11.21 \pm 0.76$	$15.0 \pm 1.3$	$0.25 \pm 0.11$	$(1.46 \pm 0.08) \times 10^{-3}$
Exo/H+He	$1.47 \pm 0.51$	$11.24 \pm 0.55$	$14.5 \pm 2.1$	$0.29 \pm 0.15$	$(5.58 \pm 0.39) \times 10^{-2}$
Alt/H+He	$1.34 \pm 0.31$	$12.02 \pm 0.58$	$14.6 \pm 0.8$	$0.23 \pm 0.09$	$(1.55 \pm 0.06) \times 10^{+2}$
Alt/Exo/H+He	$1.34 \pm 0.33$	$11.48 \pm 0.68$	$14.1 \pm 1.2$	$0.24 \pm 0.09$	$(1.84 \pm 0.07) \times 10^{+1}$

NOTE.—The first column is the model label, columns 2 through 5 give the mean and standard deviation for all five neutron stars, and column 6 is the integral for computing the Bayes factor.

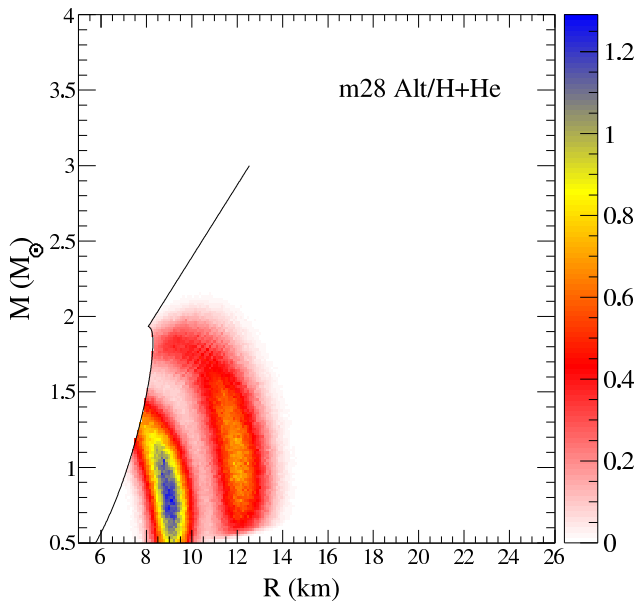


Fig. 4.— Probability distribution for  $M$  and  $R$  for the neutron star in M28 assuming the adjusted  $N_H$  value, but allowing the composition of the atmosphere to be either hydrogen or helium.

ues of  $N_H$ , we can use the ratio

$$\frac{B_{\text{Alt}} + B_{\text{Exo/Alt}}}{B_{\text{Base}} + B_{\text{Exo}}} \approx \frac{B_{\text{Exo/Alt}}}{B_{\text{Exo}}} = (8.5 \pm 1.5) \times 10^4. \quad (19)$$

Unless some other systematic uncertainty is confounding this analysis, this is decisive evidence that the alternate  $N_H$  values are preferred over the Hydrogen column densities G13 obtained by fitting the X-ray spectrum. The inferred pressure–energy density relations with the alternate values of  $N_H$ , are given in Fig. 8.

### 6.3. Simulations with both H and He Atmospheres

We now consider models with the alternate assumptions about  $N_H$ , but also allow for the possibility that any source, with the exception of  $\omega$  Cen, could have a helium rather than a hydrogen atmosphere (Alt/H+He). The EOS and  $M - R$  relation are computed in the same way as before, and the associated Bayes factors can be easily computed from the results in Table 4. In this case, since  $B_{\text{Alt/Exo/H+He, Alt/H+He}} \sim 1/10$ , there is now a strong preference for matter without strong phase transitions. This is perhaps unsurprising since larger radii are implied by helium atmospheres and strong phase transitions are more compatible with small radii. The best fit is clearly obtained with no restrictions on the composition of the atmosphere and with the alternate  $N_H$  val-

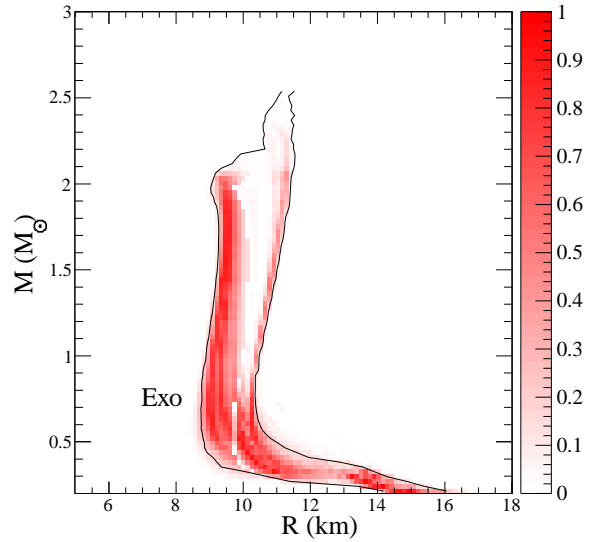
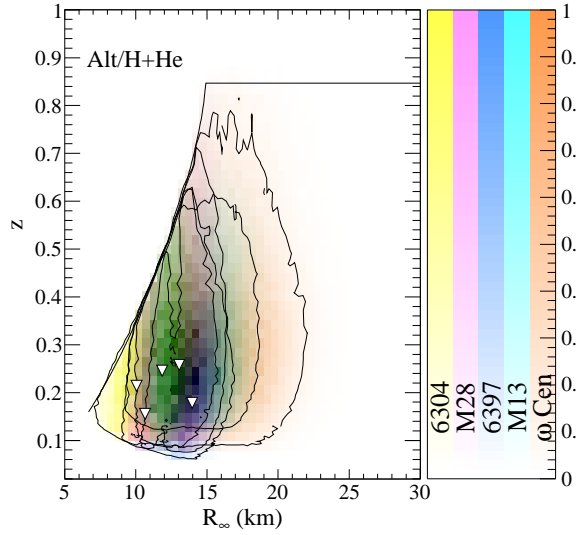
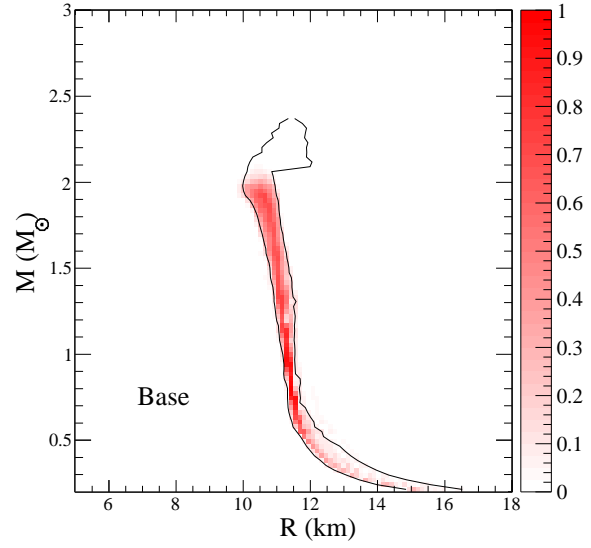
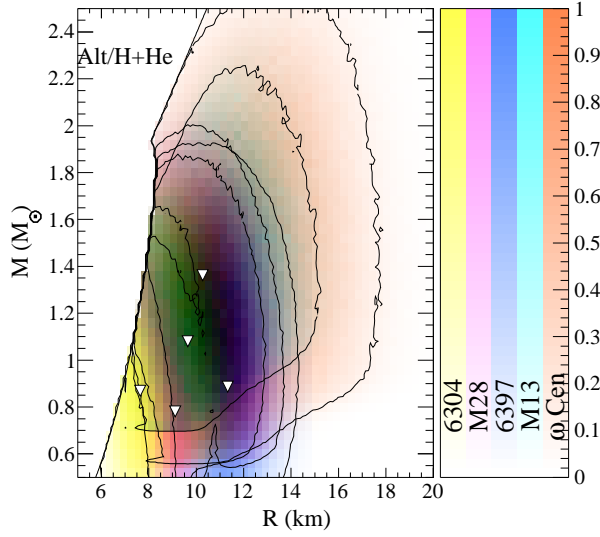


Fig. 5.— Probability distributions in the  $(z, R_\infty)$  and  $(M, R)$  planes assuming the adjusted  $N_H$  value, but allowing the composition of the atmosphere to be either hydrogen or helium. A black and white version is given in an Appendix at the end.

Fig. 6.— The probability distributions for mass as a function of radius for neutron stars assuming the baseline EOS (top panel) or a model which favors strong phase transitions (bottom panel) based on the QLMXB data from G13.

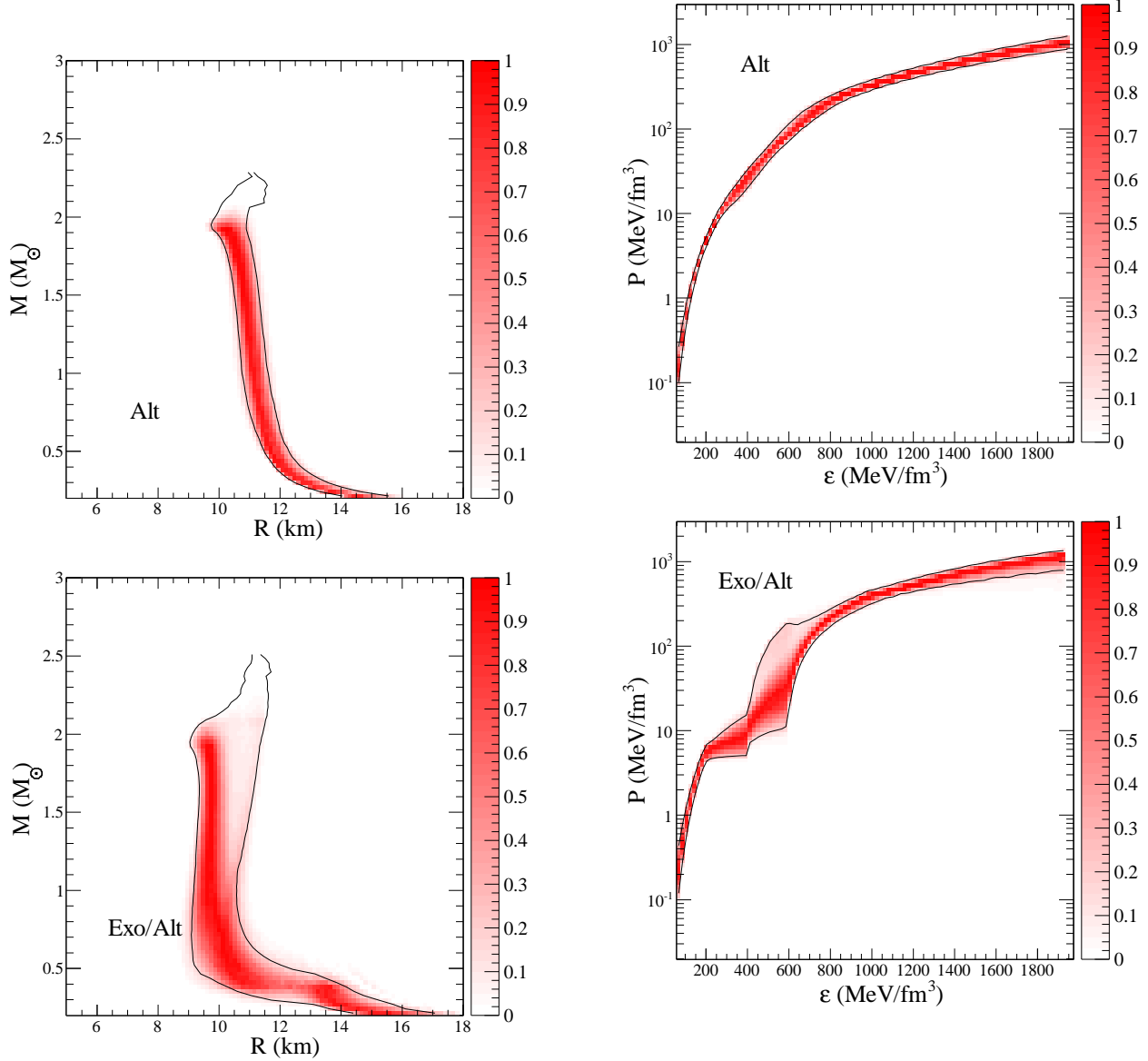


Fig. 7.— The probability distributions for mass as a function of radius for neutron stars for the baseline EOS (top panel) and for the EOS with strong phase transitions based on the QLMXB data from G13 after the correction to  $R_\infty$ .

Fig. 8.— The probability distributions for the pressure as a function of energy density corresponding to the QLMXB data from G13 after the  $R_\infty$  correction due to the alternate  $N_H$  values. The top panel displays results for model A and the bottom for model C. The kinks in the bottom panel are the result of phase transitions which allow the radius to be smaller for smaller mass neutron stars.

ues. This best fit is obtained when the neutron stars in M28 and NGC 6304 both contain helium atmospheres. The associated EOS and  $M - R$  curves are given in Fig. 9. The radius of a  $1.4 M_{\odot}$  neutron star is between 11.4 and 12.1 km (68%) and 10.4 to 12.8 km (95%). These radii are similar to those that one expects from the PRE X-ray sources Steiner, Lattimer & Brown (2013). However, these conclusions depend on assumptions about  $N_H$ . If a future study were to confirm larger values of  $N_H$  for M28 and NGC 6304, then helium atmospheres would not necessarily be preferred for the two neutron stars in these clusters.

## 7. DISCUSSION AND CONCLUSIONS

Our results show that models employing independently determined values for  $N_H$  are strongly favored over models that use  $N_H$  values self-consistently derived as part of the spectral fitting procedure. We also find that allowing the possibility of either hydrogen or helium atmospheres is strongly favored by the currently available mass and radius data from QLMXBs. In this case, the combination of independently-determined  $N_H$  values and the possibility of either H or He atmospheres, the EOS of dense matter is strongly favored to not contain strong phase transitions, such as those due to the quark-hadron phase transition. However, if all sources are eventually shown to possess hydrogen atmospheres, the EOS is then strongly favored to have strong phase transitions.

In our most-favored model, the most likely neutron star radii, 10.3–13.2 km (for stars between 0.8 and 2 solar masses), are spectacularly consistent with the predicted radius range for  $1.4 M_{\odot}$  stars from nuclear experimental (Newton et al. 2011; Tsang et al. 2012; Lattimer & Lim 2013) and theoretical neutron matter studies (Steiner & Gandolfi 2012; Hebeler et al. 2013), about 10.7–13.1 km and 10 – 13.7 km, respectively, with all confidence regions being 90%

However, the uncertainties in  $N_H$  might be quite large. The analysis from G13 suggests that the ratio of  $N_H$  values determined from spectral fitting to those from HI surveys can range from 1/2 to 2. In the context of mass and radius observations, this uncertainty has enormous implications. Our work should motivate more extensive observations in several wavelength regimes to

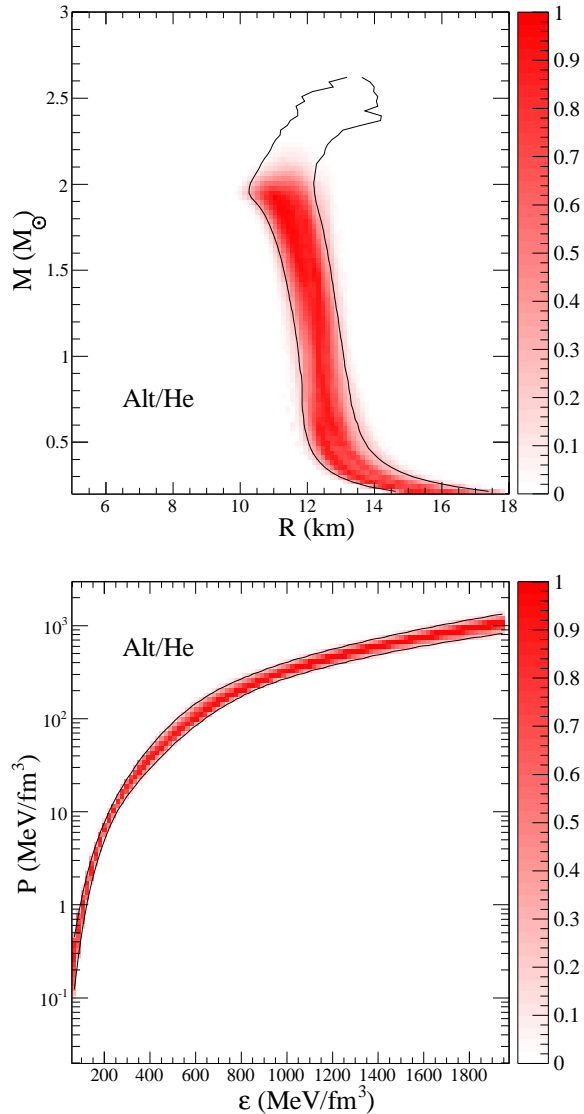


Fig. 9.— Mass-radius (top panel) and EOS probability distributions (bottom panel) for radius for neutron stars assuming the baseline EOS, with alternate set of column densities and allowing for hydrogen or helium atmospheres.

determine  $N_H$  along the lines of sights to globular clusters with more precision. In the radio, more detailed measurements of HI column densities and metallicities of intervening matter are possible with present technologies. In X-rays, however, the problem is more challenging because large throughput detectors with high spectral resolution at low energies (0.1 - 0.3 keV) is required to determine column densities directly through observations of edges in the spectrum. It is possible that observations of bright X-ray bursts from these clusters could provide the required information. The absolute flux calibration of X-ray detectors could also shift radius measurements in either direction by as much as 15%. Distance uncertainties are still in the neighborhood of 10% and should be improved. Finally, better X-ray data is needed to determine the compositions of accreting neutron stars in QLMXB systems, as this can make 30% or greater changes in inferred neutron star radii.

There are also systematic uncertainties in the probability distributions for neutron star radii, the EOS, and for the Bayes factors coming from the choice of the prior distribution. The choice of prior manifests itself in two ways: the selection of the EOS parameterization, and the choice of the neutron star mass function. The effect of the EOS parameterization could be analyzed more systematically, e.g. through a hierarchical analysis, but this would require a large computational effort beyond the scope of this work. The neutron star mass function could also be varied, in line with recent progress in mass measurements (Lattimer 2012) and this will be pursued in future work. Assuming that neutron stars of low mass are more probable will tend to prefer smaller values of  $R_\infty$ , because causality and the maximum mass constraint tend to prefer  $M-R$  curves which are vertical (i.e. fixed  $R$ ) in the region of interest. This could provide evidence in favor of strong phase transitions and H atmospheres.

One final possibility is that the low-mass X-ray binary systems studied here contain strange quark stars rather than neutron stars. This conclusion could be consistent with the relatively small range of redshifts and small radii obtained for some of the QLMXBs. The large radius inferred for  $\omega$  Cen by G13 disfavors a quark star interpretation, but a quark star model might be a good fit to the data assuming that our alternate  $N_H$  values

are correct. On the other hand, it is difficult for strange quark stars to reproduce the wide array of phenomenology observed in LMXBs including X-ray bursts, superbursts (Page & Cumming 2005), and crust cooling (Stejner & Madsen 2006). Furthermore, if the neutron star maximum mass is substantially higher than  $2 M_\odot$ , as perhaps indicated by the two black widow pulsar systems PSR B1957+20 (van Kerkwijk, Breton and Kulkarni 2011) and PSR J1311-3430 (Romani et al. 2012), as well as the binary pulsar J1748-2021B in NGC 6440 (Freire et al. 2008), the possibility of strange quark stars is strongly disfavored.

This work is supported by DOE grants DE-AC02-87ER40317 (J.M.L.) and DE-FG02-00ER41132 (A.W.S.). We thank E. Brown, S. Guillot and S. Reddy for discussions, S. Guillot for providing data from G13, and E. Brown bringing to our attention the analytic approximation for hydrogen atmospheres, Eq. (8), and its derivation in §3.2.

## APPENDIX A: RESCALING $R_\infty$ FOR THE NEUTRON STAR IN $\omega$ CEN

G13 obtained a large value for  $R_\infty$  in the case of  $\omega$  Cen because they deduced a large value for  $N_H$ . Their probability distributions were confined to  $M < 3 M_\odot$ , which effectively decreases to  $M < 1.8 M_\odot$  when  $R_\infty$  is corrected by the factor of 0.511 for our lower alternative value of  $N_H$  as given in Table 2. This missing information creates an unphysical constraint on the mass of the neutron star when computing the corrected  $R_\infty$  distribution. We therefore simulate data for  $M > 1.8 M_\odot$  in this case using the same distribution in  $z$  and  $R_\infty$  as that inferred from G13 in the region  $R_\infty < 23.02$  km, the region unaffected by the  $M < 3 M_\odot$  limit. The simulated data is added to the original G13 data and the sum is renormalized to ensure that the probability distribution is smooth across the  $M = 1.8 M_\odot$  boundary.

## APPENDIX B: BLACK AND WHITE FIGURES

Figures 10-12 are the same as Figures 1, 3 and 5, respectively, except that (i) probability density is represented on a grayscale, (ii) different line patterns are used to represent the five different sources, and (iii) regions where the probability

density is less than that given by the 90% confidence limit are not plotted.

## REFERENCES

- J. Antoniadis et al., *Science* 340, 448 (2013)
- W. Becker, D. A. Swartz, G. G. Pavlov, R. F. Elsner, J. Grindlay, R. Mignani, A. F. Tennant, D. Backer, L. Pulone, V. Testa and M. C. Weiskopf, *ApJ*, 594, 798 (2003)
- L. Bildsten, E. E. Salpeter and I. Wasserman, *ApJ* 384, 143 (1992)
- E. F. Brown, L. Bildsten and R. E. Rutledge, *ApJ Lett.* 504, L95 (1998)
- A. Catuneanu, C. O. Heinke, G. R. Sivakoff, W.C. G. Ho, and M. Servillat, *ApJ* 764, 145 (2013)
- P. B. Demorest, T. Pennucci, S. M. Ransom, M. S. E. Roberts and J. W. T. Hessels, *Nature* 467, 1081 (2010)
- J. M. Dickey and F. J. Lockman, *Annu. Rev. Astron. Astrophys.* 28, 215 (1990)
- P. C. C. Freire, S. M. Ransom, S. Bégin, I. H. Stairs, J.W. T. Hessels, L. H. Frey and F. Camilo, *ApJ* 675, 670 (2008)
- P. C. C. Freire et al., *MNRAS* 412, 2763 (2011)
- B. Gendre, D. Barret and N. A. Webb, *Astron. Astrophys.* 400, 521 (2003a)
- B. Gendre, D. Barret and N. A. Webb, *Astron. Astrophys.* 403, L11 (2003b)
- S. Guillot, R. E. Rutledge, L. Bildsten, E. F. Brown, G. G. Pavlov and V. E. Zavlin, *MNRAS* 392, 665 (2009)
- S. Guillot, R. E. Rutledge and E. F. Brown, *ApJ* 732, 88 (2011a)
- S. Guillot, R. E. Rutledge, E. F. Brown, G. G. Pavlov and V. E. Zavlin, *Astropys. J.* 738, 129 (2011b)
- S. Guillot, M. Servillat, N. A. Webb and R. E. Rutledge, *arXiv:1302.0023* (2013)
- T. Güver, F. Özel, A. Cabrera-Lavers and P. Wroblewski, *ApJ* 712, 964 (2010)

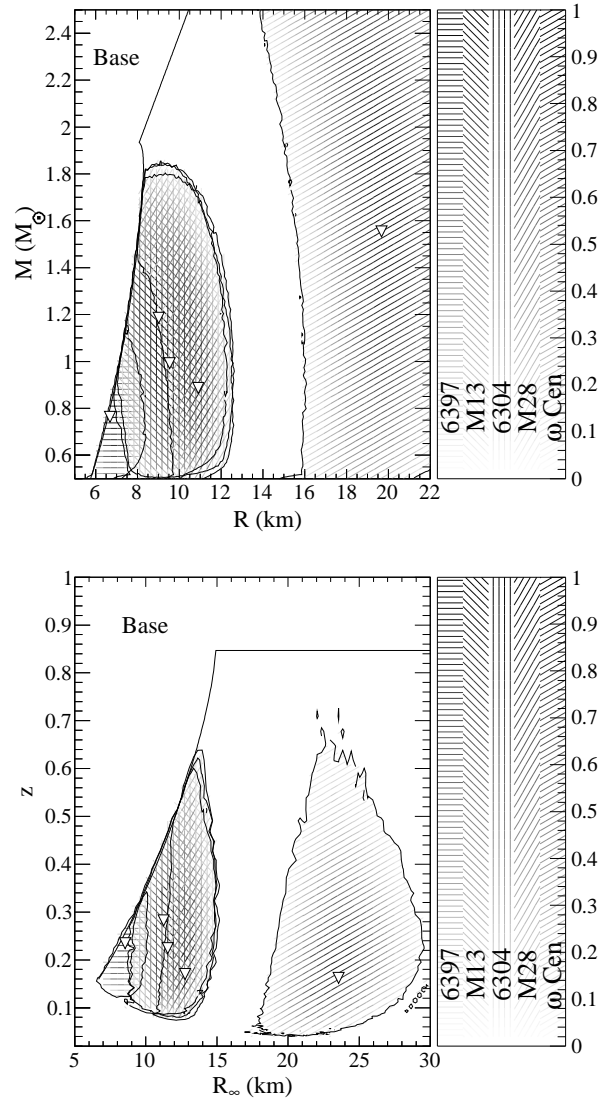


Fig. 10.— 90% error contours in  $R_\infty$  and  $z$  (top panel) and  $M$  and  $R$  (bottom panel) for quiescent low-mass X-ray binaries studied by G13. Triangles mark the best-fit values and contour lines give the 90% confidence regions. The regions to the left of or above the solid lines are forbidden by the combination of causality and a  $1.93 M_\odot$  lower limit to the neutron star maximum mass. The probability density is represented in a grayscale with a different fill pattern for each of the five neutron stars.

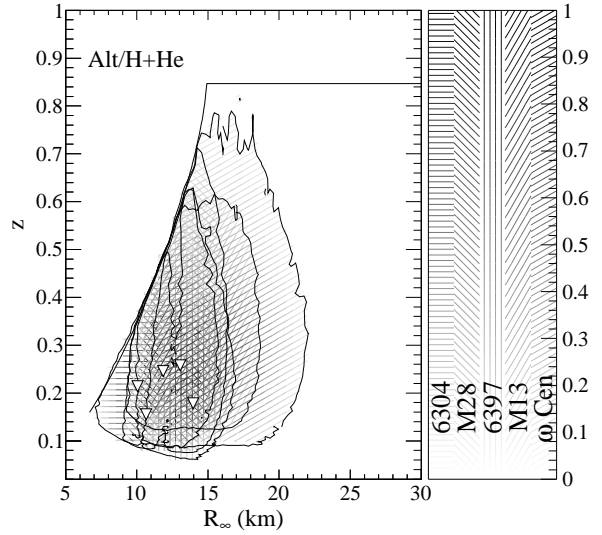
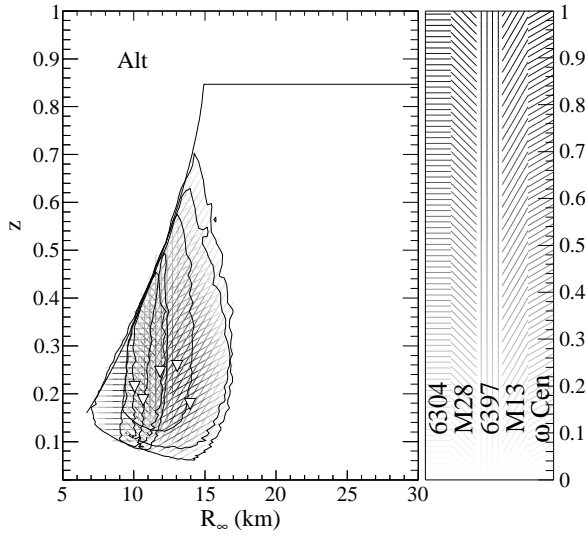
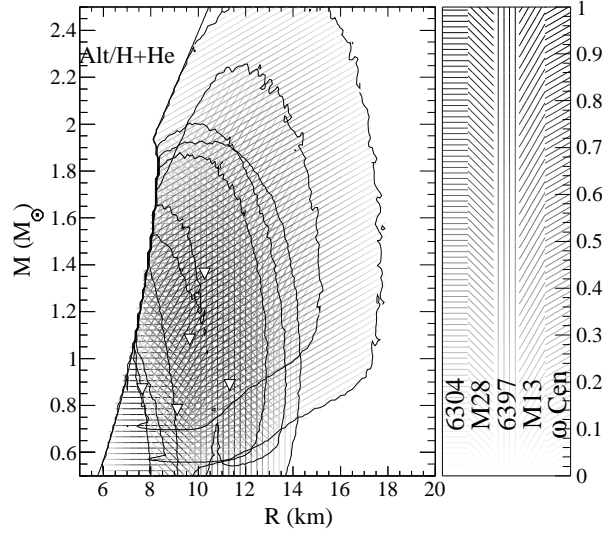
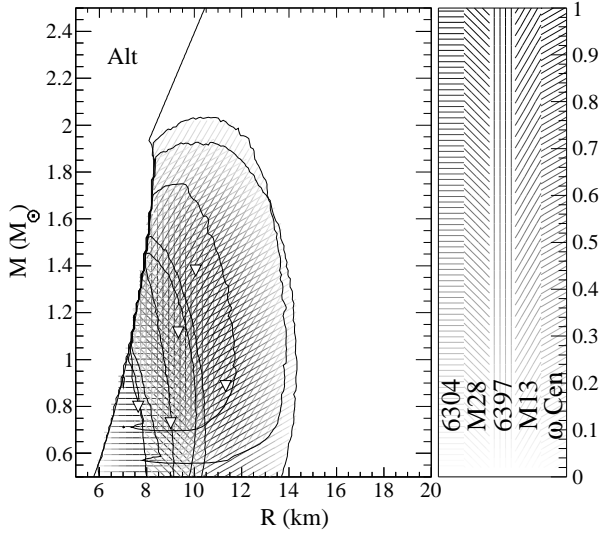


Fig. 11.— Similar to Fig. 1, but employing  $N_H$  values from Dickey & Lockman (1990) and the interpolation to scale  $R_\infty$  described in the text.

Fig. 12.— Probability distributions in the  $(z, R_\infty)$  and  $(M, R)$  planes assuming the adjusted  $N_H$  value, but allowing the composition of the atmosphere to be either hydrogen or helium.

- T. Güver, P. Wroblewski, L. Camarota and F. Özel, *ApJ* 719, 1807 (2010)
- C. B. Haakonsen, M. Turner, N. A. Tacik and R. E. Rutledge, *ApJ* 749, 52 (2012)
- D. Haggard, A. M. Cool, J. Anderson, P. D. Edmonds, P. J. Callanan, C. O. Heinke, J. E. Grindlay and C. D. Bailyn, *ApJ* 613, 512 (2004)
- K. Hebeler, J. M. Lattimer, C. J. Pethick and A. Schwenk, arXiv:1303.4662 (2013)
- C. O. Heinke, J. E. Grindlay and P. D. Edmonds, *ApJ* 622, 556 (2005)
- C. O. Heinke, G. B. Rybicki, R. Narayan and J. E. Grindlay, *ApJ* 644, 1090 (2006)
- J. M. Lattimer, *Annu. Rev. Nucl. Part. Sci.* 62, 485 (2012)
- J. M. Lattimer and Y. Lim, *ApJ*, in press (2013); arXiv1203.4286
- J. M. Lattimer and M. Prakash, *ApJ* 550, 426 (2001)
- J. M. Lattimer and M. Prakash, *Phys. Rep.* 442, 109 (2007)
- W. H. G. Lewin, J. van Paradijs and R. E. Taam, *Sp. Sci. Rev.* 62, 223 (1993)
- J. E. McClintock, R. Narayan and G. B. Rybicki, *ApJ* 615, 402 (2004)
- W. G. Newton, M. Gearheart, J. Hooker and B.-A. Li, in "Neutron Star Crust", ed. C. A. Bertulani and J. Piekarewicz, arXiv:1112.2018 (2011)
- F. Özel, G. Baym and T. Güver, *Phys. Rev. D.* 82, 101301 (2010)
- F. Özel, A. Gould and T. Güver, *ApJ* 748, 5 (2011)
- F. Özel, T. Güver and D. Psaltis, *ApJ* 693, 1775 (2009)
- D. Page & A. Cumming, *ApJL* 635, 157 (2005)
- M. Rajagopal and R. W. Romani, *ApJ* 461, 327 (1996)
- S. Rappaport, C. P. Ma, P. C. Joss & L. A. Nelson, *ApJ* 322, 842 (1987)
- J. S. Read, B. D. Lackey, B. J. Owen and J. L. Friedman, *Phys. Rev. D* 79, 124032 (2009)
- R. W. Romani, *ApJ* 313, 718 (1987)
- R. W. Romani, A. V. Filippenko, J. M. Silverman, S. B. Cenko, J. Greiner, A. Rau, J. Elliott and H. J. Pletsch, *ApJ* 760, L36 (2012)
- R. E. Rutledge, L. Bildsten, E. F. Brown, G. G. Pavlov and E. V. Zavlin, *ApJ* 514, 945 (1999)
- R. E. Rutledge, Bildsten, L., Brown, E. F., Pavlov, G. G. and Zavlin, V. E., *ApJ* 529, 985 (2000)
- R. E. Rutledge, Bildsten, L., Brown, E. F., Pavlov, G. G. and Zavlin, V. E., *ApJ* 578, 405 (2002)
- M. Servillat, C. O. Heinke, W. C. G. Ho, J. E. Grindlay, J. Hong, M. van den Berg and S. Bogdanov, *MNRAS* 423, 1556 (2012)
- A. W. Steiner, J. M. Lattimer and E. F. Brown, *ApJ* 722, 33 (2010)
- A. W. Steiner and S. Gandolfi, *Phys. Rev. Lett.* 108, 081102 (2012)
- A. W. Steiner, J. M. Lattimer and E. F. Brown, *ApJ Lett.* 765, 5 (2013)
- M. Stejner & J. Madsen, *A&A* 458, 523 (2006)
- L. Stella, W. Priedhorsky, and N. E. White, *ApJ Lett.* 312, 17 (1987)
- V. Suleimanov, J. Poutanen and K. Werner, *Astron. & Astrophys.* 527, A139 (2011)
- M. B. Tsang, J. R. Stone, F. Camera, P. Danielewicz, S. Gandolfi, K. Hebeler, C. J. Horowitz, J. Lee, W. G. Lynch, Z. Kohley, R. Lemmon, P. Moller, T. Murakami, S. Riordan, X. Roca-Maza, F. Sammarruca, A. W. Steiner, I. Vidana & S. J. Yennello, *Phys. Rev. C* 86, 015803 (2012)
- M. H. van Kerkwijk, R. P. Breton and S. R. Kulkarni, *ApJ* 728, 95 (2011)
- J. van Paradijs, *ApJ* 234, 609 (1979)
- N. A. Webb and D. Barret, *ApJ* 671, 727 (2007)
- Wilms, J., Allen, A., McCray, R. 2000, *ApJ* 542, 914

V. E. Zavlin, G. G. Pavlov and Yu. A. Shibano,  
Astron. & Astrophys. 315, 141 (1996)

---

This 2-column preprint was prepared with the AAS L<sup>A</sup>T<sub>E</sub>X  
macros v5.2.